PAPER

Check for updates

Gold–tin co-sensitized ZnO layered porous nanocrystals: enhanced responses and anti-humidity

Ming-Shui Yao,[ab] Lin-An Cao,[b] Guo-Lin Hou,[a] Min-Lan Cai,[b] Jing-Wei Xiu,[b] Chen-Hao Fang,[b] Fang-Li Yuan [iD] *[a] and Yun-Fa Chen[a]

High responses and good selectivity are key sensing properties of metal oxide (MOX) gas sensors. However, it is still a major challenge for a single MOX gas sensor to achieve both of them. Specially, the research in the field of high performance gas sensors has been hindered by negative effects of the typical interference, relative humidity (RH). In this paper, we report the successful preparation of gold–tin co-sensitized ZnO layered porous nanocrystals (Au–5Sn–ZLPCs) *via* a sequential solvothermal reaction and deposition-reduction method. Based on Sn dopants sensitized ZLPCs, the introduction of Au decoration can act as a secondary sensitized element on the crystal surfaces of ZnO. The special synergy between noble metals and oxides can introduce additional catalytic effects to further improve sensing properties. As a result of Au–Sn co-sensitization, sensing properties of sensors towards reducing VOC gas were significantly enhanced, while those towards oxidizing ozone gas were different to each other. Besides the typical sensing properties including responses, operating temperature, response & recovery properties, *etc.*, Au–Sn co-sensitized samples significantly reduced negative effects of RH on responses to both reducing and oxidizing gases (good anti-humidity).

1. Introduction

Metal oxide (MOX) semiconductors, such as ZnO, SnO$_2$, In$_2$O$_3$, TiO$_2$ and WO$_3$, are the primary materials for chemiresistor gas sensors due to their low cost, portability, real-time operability and ease of use.[1–4] Together with nanotechnology, they help people to see invisible things *via* nano-structured/modified MOX sensors acting as the nose to detect analytic gases including toxic volatile organic compounds (VOCs) and ozone gas.[5] Since good repeatability, long-term stability and fast response & recovery are easy targets for chemiresistor MOX sensors to achieve; high responses and good selectivity have been deeply studied as the key sensing properties. However, it is still a major challenge for a single MOX gas sensor to achieve both of them. Specially, the research in the field of high performance gas sensors has been hindered by negative effects of the typical interference, relative humidity (RH).[6–12]

To find a suitable solution, numerous hierarchical structures with enhanced gas diffusion properties (utility factor[13]) have been introduced to MOX sensors in the past few years, including nanowires assembled polyhedrons or films,[14,15]

single/multi-shell hollow porous spheres,[16–18] complicated structures based on precursors (*e.g.* layered salts, metal organic frameworks (MOFs)),[19–21] nanotube arrays,[22] *etc.* MOX nanocrystals with controlled crystal surfaces were also synthesized to improve the surface reaction between target gas molecules and surface absorbed oxygen ions.[23–25] To further improve sensing properties (*e.g.* responses, selectivity, operating temperature, response & recovery), the crystal surfaces of MOX sensing materials were modified (receptor function[13]). Among those excellent works, heterostructural nanostructures (p–p, n–n, or p–n junctions),[3,6,26–29] lattice substituting doping,[30–33] and noble metal decoration[8,10,33–35] were proved to be ideal methods.

In our previous work, Sn doped ZnO layered porous nanocrystals (Sn–ZLPC) with enhanced gas diffusion and modified crystal surfaces were found to significantly improve sensing properties to VOCs gases compared with bare ZnO gas sensors.[36] However, sensing properties of Sn–ZLPCs for benzene gas are still out of the reach of an ideal gas sensor with high responses and low energy consumption. Moreover, effects of the typical interference of MOX gas sensor, relative humidity (RH), should be taken into account for practical application including reliable breath analysis, indoor detection, wearable devices, *etc.*[6–11] Based on Sn dopants sensitized ZLPCs, the introduction of noble metal decoration can act as a secondary sensitized element on the crystal surfaces of ZnO. The special synergy between noble metals and oxides can introduce additional catalytic effects to further improve sensing properties, which

[a]State Key Laboratory of Multi-Phase Complex Systems, Institute of Process Engineering, Chinese Academy of Sciences, Zhongguancun Beiertiao 1 Hao, Beijing, 100190, P. R. China. E-mail: flyuan@ipe.ac.cn

[b]State Key Laboratory of Structural Chemistry, Fujian Institute of Research on the Structure of Matter, Chinese Academy of Sciences, Fuzhou, 350002, P. R.China

might be the ideal candidate to address issues mentioned above.

In this paper, we demonstrate the synthesis and applications of Au–Sn co-sensitized ZnO layered porous nanocrystals (Au–Sn–ZLPCs). The synthesized Au–Sn–ZLPCs performed excellent sensing properties to VOCs and ozone due to the combination of catalytic effects of Au–Sn, modified crystal surfaces and the mesoporous hierarchical structure. Specially, high responses, low operating temperature, and good anti-humidity (free of the RH interference) can be realized.

2.   Materials and methods

2.1   Synthesis of Sn doped ZnO layered porous nanocrystal (Sn–ZLPC)

The synthesis of 5.0 at% Sn–ZLPC can be found in our previous work.[36] Briefly, 1.000 g $ZnAc_2 \cdot 2H_2O$ and 0.052 g $SnCl_2 \cdot 2H_2O$ were added to 10 mL de-ionized water under stirring. Then 60 mL glycerol was added slowly to the mixture under vigorous stirring. 30 min later, the resulting solution was transferred to a Teflon-lined 100 mL stainless steel autoclave and maintained at 200 °C for 8 h before cooling down to room temperature. After that, the particles were collected from the bottom of the reactor and washed three times with de-ionized water and twice with ethanol by re-dispersion and centrifugation (4500 rpm for 10 min each time). The solid materials were then dried in air at 60 °C for 12 h.

2.2   Synthesis of Au decorated Sn–ZLPC

Before Au decoration, Sn–ZLPC was heated at 500 °C for 2 h and then 400 °C for 20 h. After calcination, 0.1 g 5.0 at% Sn–ZLPC was added to 40 mL aqueous solution containing equal-molar $HAuCl_4$ and sodium citrate (0.25 mM for Au–5Sn–ZLPC-1, and 2.5 mM for Au–5Sn–ZLPC-2) under stirring. Then 0.63 mL 0.50 M $NaBH_4$ aqueous solution was added to it under stirring. After 30 min, the particles were collected from the bottom of the reactor and washed three times with de-ionized water and twice with ethanol by re-dispersion and centrifugation. The solid materials were then dried in air at 60 °C for 12 h.

2.3   Materials characterization

The phase and crystal structure of the product were determined by X-ray diffraction (XRD) patterns, which were recorded with a Philips X'Pert PRO MPD X-ray diffractometer using Cu Kα radiation ($\lambda = 1.54178$ Å). The morphology and structure of the product were then observed by scanning electron microscope (SEM, JEOL JSM-6700F) and transmission electron microscope (TEM, JEOL JEM-2100). The thermal behavior of Sn–ZLPC was examined by thermogravimetry-differential thermal analysis (TG-DTA) with a NETZSCH STA 449C analyzer using a heating rate of 5 °C min^{-1} in flowing air ambient (60 sccm). The surface chemical analysis was investigated by X-ray photoelectron spectroscopy (XPS) on a Thermo Scientific ESCALAB 250 Xi XPS system, where the analysis chamber was 1.5×10^{-9} mbar and the size of X-ray spot was 500 μm.
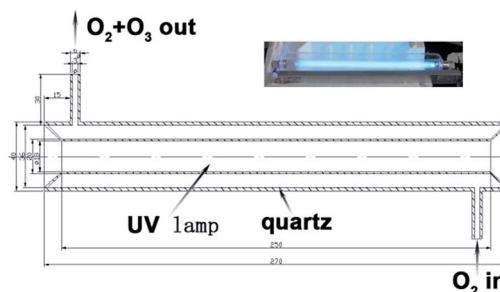

Fig. 1   Schematic diagram (the cross-sectional view) of the experimental set-up used to produce ozone gas (the inset is a digital photograph of the experimental set-up).

2.4   Fabrication of gas sensor prototype and sensor characterization

The fabrication of gas sensor prototypes and the sensor characterization were reported in our previous works.[19,25] Bare 5Sn–ZLPC was heated at 500 °C for 2 h and then 400 °C for 20 h before sensor fabrication. The solution containing sensing material and ethanol was drop-coated onto the Al_2O_3 substrate with two electrodes wires on both ends. Preheating at 550 °C for 60 min before the achievement of stable process (400 °C for 20 h) was needed to ensure good ohmic contact. VOC gas was introduced into the quartz tube by mixing the certified gas "mixtures" and dry air in the proper ratio controlled by the mass flow controllers.[37] Ozone gas was generated by a home-made instrument irradiated by an UV-light as showed in Fig. 1 and the corresponding description. The constant flow was 600 mL min^{-1}. The bias on the sensor was 10 V, and the current was recorded using Keithley 2601 Sourcemeter. The response to VOCs was defined as the ratio of sensor resistance in air and in detected gas ($R_{air}/R_{gas} - 1$). The response to ozone was defined as the ratio of sensor resistance in air and in detected gas ($R_{gas}/R_{air} - 1$). The response/recovery time is defined as the time required for the resistance of the sensor to change to 90%/10% of the saturation value after exposure to the test gas/air.

High purity oxygen was irradiated by an 8 W UV light (186 nm) to obtain a mixture of O_2 and O_3. By mixing it with high purity oxygen and high purity nitrogen, synthetic air (79% N_2 and 21% O_2) with different concentrations of ozone can be obtained (0.09 to 1.07 ppm for UV light coated by layer of Teflon film with a thickness of 0.1 mm, and 2 to 16 ppm for bare UV light).

3.   Results and discussion

3.1   Materials preparation and characterization

XRD patterns of 5 at% Sn-doped ZnO powders are presented in Fig. 2(a). These patterns correspond to three main diffraction peaks of hexagonal wurtzite ZnO (JCPDS 01-089-0510), namely (100), (002) and (101).

The intensities of diffraction peaks in the PXRD of 5Sn–ZLPC are rarely affected at high temperature, indicating that the crystalline nature of the material retains at high temperature. In addition, no new peaks of a secondary phase were observed on all of the samples. As discussed in our previous work,[36] 5 at% of
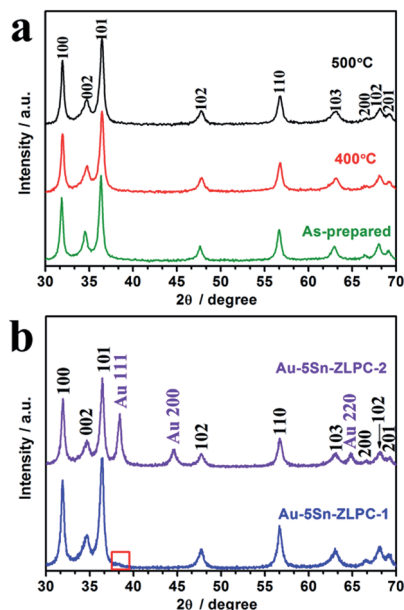
Fig. 2 XRD patterns of 5 at% Sn–ZLPC (a) treated at different temperature and (b) decorated with different amounts of Au nanocrystals.

Sn doping slightly shifts the position of (002) peaks from 36.311° (pure ZnO) to higher diffraction angles (36.361°), which due to its smaller radius. It is also an evidence for the successful substitution of Sn into the ZnO lattice.

Fig. 2(b) shows typical mixed patterns of ZnO and Au (JCPDS 00-004-0784) for samples decorated with different amounts of Au nanocrystals. The diffraction peaks located at 38.4° and 64.8° were indexed to be Au (111) and Au (220), respectively.

For better understanding of the effects of heating, as-prepared 5Sn–ZLPC was examined by TG-DTA (Fig. 3). The small and wide endothermic peak with gradual mass loss from 70 to 100 °C were ascribed to the release of water molecules adsorbed in the pores and on the surface of 5Sn–ZLPC. A further mass loss in the temperature range 245–360 °C corresponded to release of residual organics. The mass loss was nearly complete at 360 °C, and we assigned the exothermic peak (296.6 °C) near
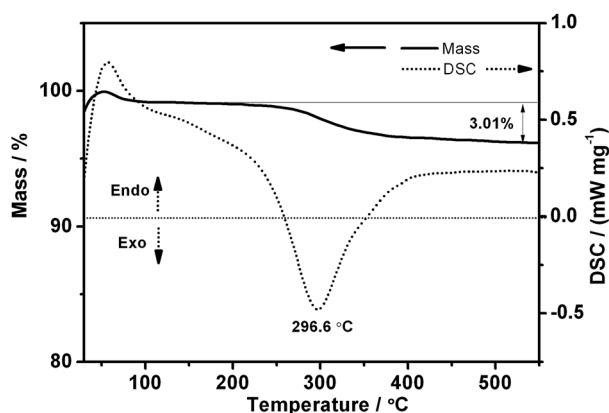
this temperature to the combustion of residual organics (the total mass loss, 3.01%). Together with combustion of residual organics based on the TG-DTA results, slightly broader peaks than as-prepared sample observed for calcinated samples might be attributed to collapse of some large nanocrystals in the layered structure. Therefore, the heating procedure used for 5Sn–ZLPC can both remove residual organics and keep good crystallinity, which is beneficial for the uniform loading of Au nanocrystals.

As discussed in our previous work,[36] Sn^{4+} doped ZnO layered nanocrystals with mesoporous hierarchical structure were formed under the effects of Ostwald ripening, together with the etching effects of halogen ions (Fig. 4). The previous structural analysis based on SEM, TEM and BET results showed that each particle was constructed by multi-layers of ZnO nanosheet (thickness, 10–20 nm), and each of such nano-sheets are constructed by and nanocrystals and nanopores (mainly of less than 10 nm).

After the removal of residual organics *via* calcination, Au nanocrystals were deposited onto the surface of 5Sn–ZLPC *via* the reduction of $HAuCl_4$ in aqueous solution. SEM and TEM images of samples loaded with different amounts of Au nanocrystals can be seen in Fig. 5. It can be seen that the morphology of 5Sn–ZLPC is maintained after Au decoration because of the mild reaction conditions and uniformly dispersed Au nanocrystals. Au elements can be observed *via* EDS results. The existence of Au nanocrystals can be confirmed by its light red color, TEM EDS results (Au/Sn/Zn 0.4/6.4/100), and HRTEM images (Fig. 5(a) and (b)). Au/Sn/Zn of Au–5Sn–ZLPC-2 was calculated to be 0.3/4.0/100 and 2.0/5.0/100 for SEM and TEM EDS results (Fig. 5(c)), respectively. HRTEM image and EDS mapping images of Au–5Sn–ZLPC-2 clearly show the successfully deposition of Au nanocrystals on Sn–ZLPC (Fig. 5(d)).

The surface/near-surface chemical composition of Au–5Sn–ZLPC was examined by X-ray photoelectron spectroscopy (XPS). The full-range XPS spectra (Fig. 6(a)) reveals that it is mainly composed of Zn, Au, Sn, O and C elements, of which C contamination can be mainly attributed to the residual solvents.

More detailed information on the chemical state of these elements can be obtained from the high resolution XPS spectra of the Au 4f, Sn 3d and O 1s. Fitting the Au 4f spectrum (Fig. 6(b)) shows gold nanoparticles to be in a single metallic state.[38,39]
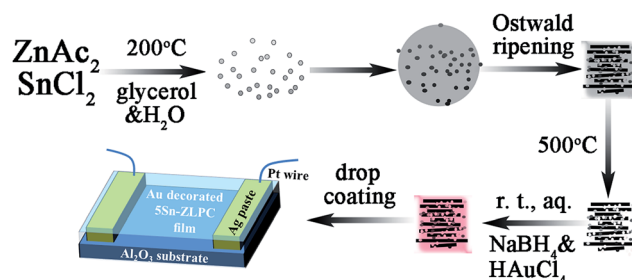

Fig. 3 TG-DTA curves of synthesized LBZA films of 5.0 at% Sn–ZLPC.

Fig. 4 Schematic illustration of the preparation of Au–5Sn–ZLPCs gas sensors.
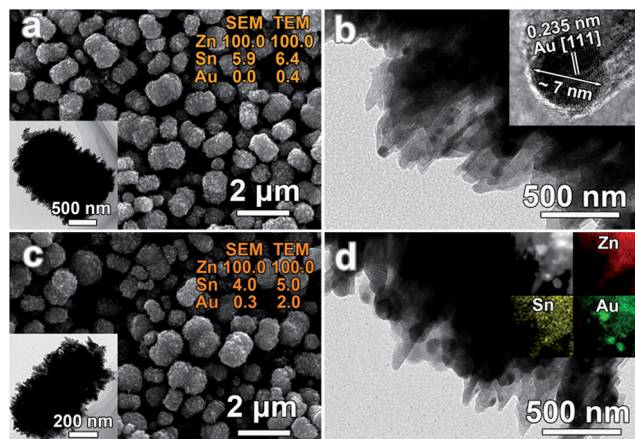
Fig. 5 SEM, TEM images and EDS results of 5.0 at% Sn–ZLPC decorated by different amounts of Au: (a, b) Au–5Sn–ZLPC-1 (insets are corresponding TEM and HRTEM images), (c, d) Au–5Sn–ZLPC-2 (insets are corresponding TEM and EDS mapping images).
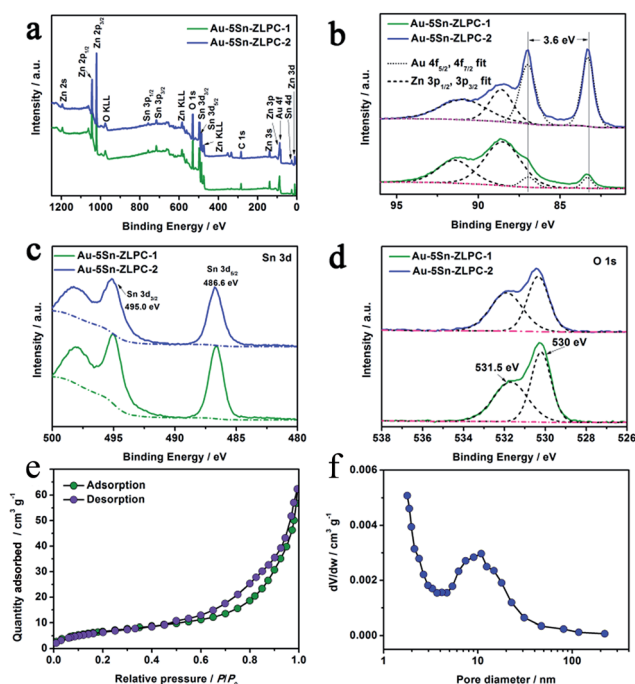

Fig. 6 (a) XPS spectra and (b–d) high resolution XPS spectra of Au–5Sn–ZLPCs at binding energies corresponding to Au 4f, Sn 3d and O 1s, respectively. (e) N_2 adsorption–desorption isotherm and (f) the BJH pore size distribution calculated from adsorption branches of Au–5Sn–ZLPC-2.

The peaks of Sn 3d3/2 and Sn 3d5/2 at 495.0 and 486.6 eV (Fig. 6(c)) can be assigned to the lattice tin (Sn(IV) oxidation state) in tin oxide,[40–42] which is consistent with bare 5Sn–ZLPC.[36] The O 1s peaks are much asymmetric. The strong peaks of non-lattice oxygen at high BE (531.5 eV) in Fig. 6(d) indicate that there are large amounts of absorbed oxygen ions on the surface of the crystal, which facilitates the gas sensing reactions. Calculated from the quantified peak area, the atomic ratio of Au/Sn/Zn was estimated to be 0/25.2/100, 7.8/19.6/100, and 22.5/

20.1/100 for bare 5Sn–ZLPC, Au–5Sn–ZLPC-1 and Au–5Sn–ZLPC-2, which is much higher than that estimated by EDS. High amount of Sn on the surface is mainly due to Sn tends to demix from the ZnO lattice because of its tendency for octahedral coordination.[36] High amount of Au can be attributed to Au nanocrystals dispersed on the surface of 5Sn–ZLPC.

The nitrogen adsorption–desorption isotherm in Fig. 6(e) exhibits type IV isotherms with type H3 hysteresis loops. According to the BJH pore size distribution curve calculated from the adsorption isotherm (Fig. 6(f)), pore diameter of Au–5Sn–ZLPC-2 mainly centered at 10 nm. The BET surface area was calculated to be 25.42 $m^2 g^{-1}$. The meso-pore and the BET surface area can be attributed to co-effects of the mesoporous structure of 5Sn–ZLPC and deposition of Au nanocrystals. The mesoporous hierarchical structure might be beneficial to the diffusion of acetone molecules.

It should be noted that Au nanoparticles formed on the surfaces of 5Sn–ZLPC and in solution can be effectively separated by setting the centrifugation speed to 4500 rpm for 10 min each time. After 3–5 circles, Au decorated 5Sn–ZLPC can be obtained at the bottom of the tube.

3.2 Sensing properties

Gas sensing processes can be divided into three units, namely, gas diffusion/molecule capture (utility factor and some case of receptor function), surface reaction (receptor function), and electron transport (transducer function).[13,19] Surface reaction unit is important for high sensing properties due to its contribution in utility factor. Noble metal decoration (Pt, Pd, Au, *etc.*) is an effective way to modify the sensing surface by enhancing the surface reaction due to its catalytic effect (high response) and the additional depletion layer (high resistance).[34,43–45]

3.2.1 VOCs. After the decoration with Au nanocrystals, the optimal operating temperature of Au–5Sn–ZLPC for benzene detection could be reduced from 475 °C to 350 °C (Fig. 7(a)). Due to the loading of Au nanoparticles, the responses to benzene of Au–5Sn–ZLPC-1 (Au/Sn/Zn 0.4/6.4/100, $R_{49.4 ppm}$ = 32.82) at 350 °C were higher than that of 5Sn–ZLPC at 475 °C ($R_{49.4 ppm}$ = 27.36) and pure ZnO without Sn doping ($R_{49.4 ppm}$ = 5.70). For Au–5Sn–ZLPC-2 (Au/Sn/Zn 2.0/5.0/100), significantly improved response ($R_{49.4 ppm}$ = 117.1) than pure sample and sample with low amounts of Au nanoparticles can be observed.

The typical response–recovery current line to VOCs with different concentration can be found in Fig. 7(b), which shows good response–recovery properties of the sample. Table 1 shows that response and recovery properties are significantly improved by the catalytic effects of Au loading on the gas sensing reaction. Co-sensitization of gold and tin can reduced the operating temperature, enhanced the responses and improved the response–recovery properties. Sn doping contributes to low activation energy, effective surface reaction based on adsorbed oxygen ions, and the mesoporous hierarchical structure. Au decoration further enhance the effective surface reaction *via* catalytic effect and the additional depletion layer, which is fully discussed by many works[34,43–45] and confirmed by results mentioned above.
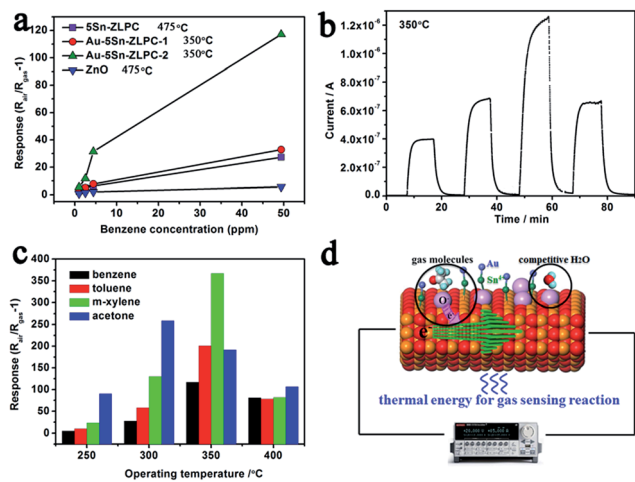
Fig. 7 Sensing properties of Au–5Sn–ZLPCs: (a) responses comparison of samples with different amounts of Au; (b) the typical response–recovery current line (50 ppm, from left to right, benzene, toluene, *m*-xylene and acetone) and (c) responses to 50 ppm VOCs at different operating temperature of Au–5Sn–ZLPC-2; (d) schematic illustration of thermal gas sensing reaction of Au decorated 5Sn–ZLPC.

Table 1 Summary of response and recovery time of different samples to 49.4 ppm benzene at 350 °C

Sample	Response time/min	Recovery time/min
5Sn–ZLPC	3.12	9.08
Au–5Sn–ZLPC-1	3.10	4.48
Au–5Sn–ZLPC-2	2.49	2.61

The temperature-dependent responses to four types of VOCs are shown in Fig. 7(c) to illustrate the relationships of the stability of target gas, operating temperature and the decoration of Au. As different thermal energies are needed to stimulate the oxidation/reduction of target gases, VOCs shows different optimal operating temperatures. As the stability of target gas increases (the ability of a gas molecule to be decomposed by adsorbed oxygen in gas sensing reactions, more difficult, more stable), the optimal operating temperature shifts from 300 °C (acetone) to 350 °C (benzene, toluene and *m*-xylene, Fig. 7(c)). For bare 5Sn–ZLPC, the gas with higher stability needs a higher thermal energy to reach its maximum response (*e.g.* benzene, 475 °C). It is known that the desorption of oxygen ions from the surface of the MOX at higher operating temperatures resulted in the reduced response.[46] The metal catalyst contributed to tune the binding energies of different adsorbates,[47,48] and thus shift the maximum response temperature and improve the response. Therefore, lower operating temperature (the adsorption rather than desorption of oxygen ions), together with the catalytic effects and additional depletion layer contribute to high response of Au–Sn co-sensitized ZLPCs (Fig. 7(d)). In addition, the responses of Au–5Sn–ZLPC-2 are comparable to other benzene sensors reported and significantly higher than the sample without noble metal decoration (Table 2).

As a typical interference of MOX gas sensor for VOC detecting, the competitive adsorption of water vapour significantly affects the sensing results (Fig. 7(d)).[8,49] More specifically, when n-type ZnO based sensing materials are exposed to VOC gas under humid atmosphere, both the water vapor and the VOC gas react with the negatively charged adsorbed oxygen and release electrons back to the semiconductor. We chose Au–5Sn–ZLPC-2 for detailed anti-humidity gas sensing measurements due to its overall good responses to benzene (high toxicity, extensive application and harmfulness even at ppb level), which is the most stable and thus the most difficult gas to be detected in this work. Due to low responses of pure ZnO, the anti-humidity property was not studied in this work. Firstly, anti-humidity properties of 5Sn–ZLPC were studied. As shown in Fig. 8(a), humidity significantly affected the responses to benzene because of the competitive adsorption of water and benzene gas molecules on the crystal surfaces. The adsorption of water molecules reduced the amounts of oxygen ions,[6–8] and thus released electrons back to ZnO, which can be confirmed by significant responses (dash line in Fig. 8(a)) and resistance decrease to pure humidity. Affected by the competitive adsorption of water molecules, higher responses at lower concentration (sub-ppm level) and lower responses at higher concentration (ppm level) can be observed, which will induce unreliable results. RH induced unreliable results exist in a wide range from 400 to 525 °C, which can be indicated by comparison of temperature-dependent responses to 49.4 ppm benzene with different RH (Fig. 8(b)).

The coefficient of variation (CV) is used to represent the effect of humidity on responses,[9] which is defined as

$$CV = R_{SD}/R_{average} \times 100\% \qquad (1)$$

where R_{SD} and $R_{average}$ are the standard deviation (SD) and average value of responses with different humidity, respectively.

After the decoration of Au, the effects of RH on responses can be reduced (CV decreased from 20–60% to 7–25%), while the fast response and recovery properties are maintained (Fig. 8(c)). Since the bind energy of adsorbed gas molecules can be affected by MOX, metal catalyst and operating temperature, it is not surprising to observe such variations as shown in Fig. 8(d). The essential goal is to find the balance point between them and obtain the operating temperature region with accetaple variation for praticle application. Comparison of temperature-dependent responses of 49.4 ppm benzene with different RH indicate that 300 °C is a suitable operating temperature for precise detection of benzene gas with different RH (CV only 5.70%, Fig. 8(d)).

The reaction of target molecules with adsorbed oxygen ions on the surface of MOX is a key unit for gas sensing, especially in a RH environments. The loading of Au nanoparticles contributes to good anti-humidity properties *via* the following two ways.[8,34,35] One is the widely accepted theory of increased surface adsorbed oxygen ions; the other is the catalytic effects on the gas sensing reaction. Both of them significantly enhanced the responses to benzene, while the resistance decrease caused by RH changes slightly. Thus the RH induced

Table 2 Benzene and acetone sensors based on undoped and doped ZnO materials reported before and in this work

Materials	Size/nm	Benzene/ppm	$R - 1$	$T_{opt}{}^a/°C$	Ref.
SnO$_2$ nanowire	80 ± 5	50	0.6	290	50
ZnO nanorod array	~8	50	9	370	51
ZnO nanosheets	Hier.^{b}	100	1	420	52
5.0 at% Sn–ZLPC	Hier.	49.4	27.4	475	36
Au–In$_2$O$_3$ nanorod	15–50	10	11.5	300	29
Pt–WO$_3$ nanoparticle	150	100	9.5	250	53
Au–Cr–WO$_3$ octahedra	100	49.8	~70	375	31
Pt–SnO$_2$	20–40	0.1	~5	400	54
Pt–ZnO flower	Hier.	44.1	~75	350	55
Au–5Sn–ZLPC	Hier.	49.4	117.1	350	This work

^{a} T_{opt} means optimal operating temperature. ^{b} Hier. means hierarchical structure.
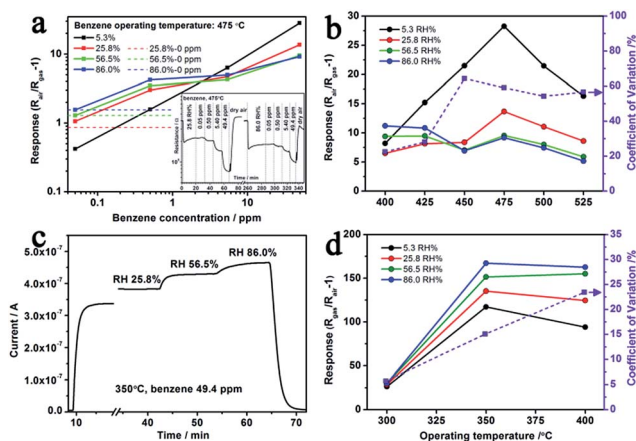

Fig. 8 Influences of humidity on the sensing properties of pure and Au decorated 5.0 at% Sn–ZLPC: (a) responses comparison to different concentrations of benzene gas (0.05, 0.5, 5.4, 49.4 ppm, dash line is the responses of humidity, the inset is the typical response–recovery resistance line under different RH) and (b) at different operating temperatures of pure 5Sn–ZLPC; (c) the typical response–recovery current line and (d) responses and the corresponding CV to 49.4 ppm benzene gas with different RH at different operating temperature of Au–5Sn–ZLPC-2.
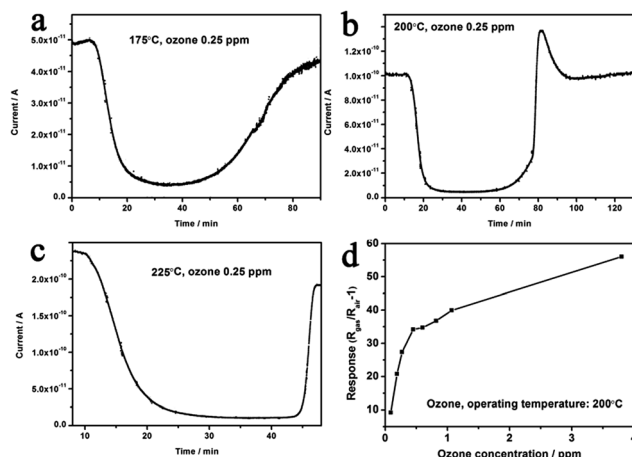

Fig. 9 Sensing properties of 5.0 at% Sn–ZLPC to ozone: (a–c) typical response–recovery current lines at different operating temperatures and (d) responses to different concentrations of ozone at 200 °C.

unreliable results can be reduced by decreasing its relative contribution to the total resistance change in the gas sensing reaction.

3.2.2 Ozone. Fig. 9(a–c) shows typical response–recovery current curves of 5Sn–ZLPC to 0.25 ppm ozone at low temperature. Since ozone is a strong oxidizing gas and thus it can capture the electrons in the conduction band of ZnO, resulting in a decreasing conductivity. Slow response and recovery time (t_{res}, 10.14 min; t_{rec}, ~30 min) to 0.25 ppm ozone were observed at 200 °C. In contrast, faster response time (t_{res}, 5.44 min) and slower recovery time (t_{rec}, ~170 min) to higher concentration of ozone (3.8 ppm) was observed, which might due to quick reach of saturated adsorption, and slow decompose & desorption of ozone at high concentration, respectively. High activity and strong oxidation of ozone enables its reaction on the surfaces of ZnO even at ppb-level concentration at low temperature. As shown in Fig. 9(d), the response to 90 ppb ozone can be up to ~10. Increasing concentrations lead to increasing responses in

a range of 0.09–3.8 ppm. For the concentration higher than 0.5 ppm, the growth of the responses becomes slow due to the saturated adsorption of ozone.

After the decoration of Au nanocrystals, response properties can be significantly improved (Fig. 10(a)). At 200 °C, the response time was reduced to ~2.60 min for Au–5Sn–ZLPC-1, while it was ~8.73 min for Au–5Sn–ZLPC-2 (Fig. 10(c)). It should be noted that catalytic effects of Au nanocrystals can decompose ozone to oxygen, which results in decreased concentration and reduced responses. As discussed above for pure 5Sn–ZLPC, low concentration of ozone will result in long response time. Thus, it might be the reason why the sample with high Au decoration showed slower response property than other samples.

The optimal operating temperature of Au–5Sn–ZLPC-2 for ozone detection could be reduced from 200 °C to 100 °C, while that of the sample with low amounts of Au nanocrystals is unchanged (225 °C, Fig. 10(b) and (d)). RH induced unreliable results (CV > 20%) were observed at some operating temperatures for two Au decorated samples. However, results at other operating temperatures show little effects by RH, of which the
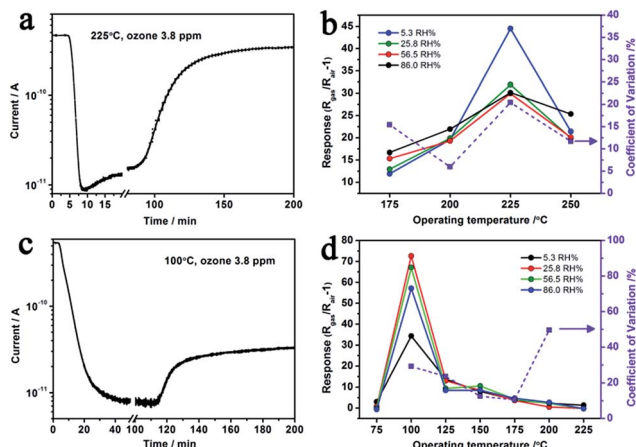
Fig. 10 Sensing properties of Au decorated 5.0 at% Sn−ZLPC to ozone and influences of humidity. (a, b) Au−5Sn−ZLPC-1 and (c, d) Au−5Sn−ZLPC-2: typical response–recovery current lines, and responses and the corresponding CV to 3.8 ppm ozone gas with different RH at different operating temperatures.

possible mechanism is similar to benzene gas mentioned above. It indicates that Au decorated samples can be used as stable ozone gas sensors at low temperature and under different RH.

4. Conclusions

In summary, the syntheses of gold–tin co-sensitized ZnO layered porous nanocrystals have been demonstrated. Sn doping contributes to low activation energy, effective surface reaction based on adsorbed oxygen ions, and the mesoporous hierarchical structure. Au decoration further enhances the effective surface reaction *via* catalytic effect and the additional depletion layer brought by the special synergy between noble metals and oxides. Co-sensitization of Au and Sn significantly enhanced sensing properties of sensors to reducing VOC gas were, while those of sensors to oxidizing ozone gas were complicated. Lower operating temperature (the adsorption rather than desorption of oxygen ions), together with the catalytic effects and additional depletion layer, contributed to enhanced sensing properties of Au–Sn co-sensitized ZnO to reducing gases. In contrast, although the response time and operating temperature were reduced, catalytic effects of Au nanocrystals can decompose ozone to oxygen, which resulted in decreased concentration and reduced responses. Apart from these typical sensing properties, (responses, operating temperature, response & recovery properties, *etc.*), Au decorated samples significantly reduced negative effects of RH on responses to both reducing and oxidizing gases (good anti-humidity). This work indicates that Au–Sn–ZLPCs can be used as stable gas sensors for both reducing and oxidizing gases at low temperature and under different RH. These interesting particles might be used for a wide range of innovative applications such as photo catalysis, the template for complex structure, electronic noses, MOX–MOFs nanocomposites, and so on.

Notes and references

1 Z. Zhao, J. Tian, Y. Sang, A. Cabot and H. Liu, *Adv. Mater.*, 2015, **27**, 2557–2582.
2 T. Wagner, S. Haffer, C. Weinberger, D. Klaus and M. Tiemann, *Chem. Soc. Rev.*, 2013, **42**, 4036–4053.
3 T. Li, W. Zeng and Z. Wang, *Sens. Actuators, B*, 2015, **221**, 1570–1585.
4 Y. Wang, Y. Zhou, C. Meng, Z. Gao, X. Cao, X. Li, L. Xu, W. Zhu, X. Peng, B. Zhang, Y. Lin and L. Liu, *Nanotechnology*, 2016, **27**, 425503.
5 J. T. Fourkas, *J. Phys. Chem. Lett.*, 2011, **2**, 2945.
6 H.-J. Kim, H.-M. Jeong, T.-H. Kim, J.-H. Chung, Y. C. Kang and J.-H. Lee, *ACS Appl. Mater. Interfaces*, 2014, **6**, 18197–18204.
7 C. Wang, L. Yin, L. Zhang, D. Xiang and R. Gao, *Sensors*, 2010, **10**, 2088.
8 N. Ma, K. Suematsu, M. Yuasa, T. Kida and K. Shimanoe, *ACS Appl. Mater. Interfaces*, 2015, **7**, 5863–5869.
9 M. S. Yao, W. X. Tang, G. E. Wang, B. Nath and G. Xu, *Adv. Mater.*, 2016, **28**, 5229–5234.
10 S.-J. C. Won-Tae Koo, S.-J. Kim, J.-S. Jang, H. L. Tuller and I.-D. Kim, *J. Am. Chem. Soc.*, 2016, **138**, 13431–13437.
11 A. T. Güntner, V. Koren, K. Chikkadi, M. Righettoni and S. E. Pratsinis, *ACS Sens.*, 2016, **1**, 528–535.
12 F. C. Chung, R. J. Wu and F. C. Cheng, *Sensors and Actuators, B: Chemical*, 2014, **190**, 1–7.
13 N. Yamazoe and K. Shimanoe, *Sens. Actuators, B*, 2009, **138**, 100–107.
14 M. R. Alenezi, S. J. Henley, N. G. Emerson and S. R. P. Silva, *Nanoscale*, 2014, **6**, 235–247.
15 T. Stoycheva, F. E. Annanouch, I. Gràcia, E. Llobet, C. Blackman, X. Correig and S. Vallejos, *Sens. Actuators, B*, 2014, **198**, 210–218.
16 S. Dilger, C. Lizandara-Pueyo, M. Krumm and S. Polarz, *Adv. Mater.*, 2012, **24**, 543–548.
17 P. Sun, X. Zhou, C. Wang, K. Shimanoe, G. Lu and N. Yamazoe, *J. Mater. Chem. A*, 2014, **2**, 1302–1308.
18 X. Zhou, W. Feng, C. Wang, X. Hu, X. Li, P. Sun, K. Shimanoe, N. Yamazoe and G. Lu, *J. Mater. Chem. A*, 2014, **2**, 17683–17690.
19 M. Yao, P. Hu, Y. Cao, W. Xiang, X. Zhang, F. Yuan and Y. Chen, *Sens. Actuators, B*, 2013, **117**, 562–569.
20 Y. Lu, W. Zhan, Y. He, Y. Wang, X. Kong, Q. Kuang, Z. Xie and L. Zheng, *ACS Appl. Mater. Interfaces*, 2014, **6**, 4186–4195.
21 W. Li, X. Wu, N. Han, J. Chen, X. Qian, Y. Deng, W. Tang and Y. Chen, *Sens. Actuators, B*, 2016, **225**, 158–166.
22 D. H. Kim, Y.-S. Shim, J.-M. Jeon, H. Y. Jeong, S. S. Park, Y.-W. Kim, J.-S. Kim, J.-H. Lee and H. W. Jang, *ACS Appl. Mater. Interfaces*, 2014, **6**, 14779–14784.

23 Y. V. Kaneti, J. Yue, X. Jiang and A. Yu, *J. Phys. Chem. C*, 2013, **117**, 13153–13162.

24 X. Han, X. Han, L. Li and C. Wang, *New J. Chem.*, 2012, **36**, 2205–2208.

25 H. Zhang, M. Yao, L. Bai, W. Xiang, H. Jin, J. Li and F. Yuan, *CrystEngComm*, 2013, **15**, 1432–1438.

26 L. Li, C. Zhang and W. Chen, *Nanoscale*, 2015, **7**, 12133–12142.

27 A. Kumar, S. Samanta, A. Singh, M. Roy, S. Singh, S. Basu, M. M. Chehimi, K. Roy, N. Ramgir, M. Navaneethan, Y. Hayakawa, A. K. Debnath, D. K. Aswal and S. K. Gupta, *ACS Appl. Mater. Interfaces*, 2015, **7**, 17713–17724.

28 S. Park, S. Kim, H. Kheel and C. Lee, *Sens. Actuators, B*, 2016, **222**, 1193–1200.

29 J. H. Kim, A. Katoch, S. H. Kim and S. K. Sang, *ACS Appl. Mater. Interfaces*, 2015, **7**, 15351–15358.

30 C. Wang, S. Ma, A. Sun, R. Qin, F. Yang, X. Li, F. Li and X. Yang, *Sens. Actuators, B*, 2014, **193**, 326–333.

31 M. Yao, Q. Li, G. Hou, C. Lu, B. Cheng, K. Wu, G. Xu, F. Yuan, F. Ding and Y. Chen, *ACS Appl. Mater. Interfaces*, 2015, **7**, 2856–2866.

32 C. Wang, X. Cui, J. Liu, X. Zhou, X. Cheng, P. Sun, X. Hu, X. Li, J. Zheng and G. Lu, *ACS Sens.*, 2016, **1**, 131–136.

33 K. Suematsu, M. Sasaki, N. Ma, M. Yuasa and K. Shimanoe, *ACS Sens.*, 2016, **1**, 913–920.

34 A. Kolmakov, D. O. Klenov, Y. Lilach, S. Stemmer and M. Moskovits, *Nano Lett.*, 2005, **5**, 667–673.

35 L. Wang, Z. Lou, T. Fei and T. Zhang, *J. Mater. Chem.*, 2012, **22**, 4767–4771.

36 M. Yao, F. Ding, Y. Cao, P. Hu, J. Fan, C. Lu, F. Yuan, C. Shi and Y. Chen, *Sens. Actuators, B*, 2014, **201**, 255–265.

37 D. Calestani, R. Mosca, M. Zanichelli, M. Villani and A. Zappettini, *J. Mater. Chem.*, 2011, **21**, 15532–15536.

38 N. Kruse and S. Chenakin, *Applied Catalysis, A: General*, 2011, **391**, 367–376.

39 M. C. Patterson, X. Nie, F. Wang, R. L. Kurtz, S. B. Sinnott, A. Asthagiri and P. T. Sprunger, *J. Phys. Chem. C*, 2013, **117**, 18386–18397.

40 M. D'Arienzo, L. Armelao, A. Cacciamani, C. M. Mari, S. Polizzi, R. Ruffo, R. Scotti, A. Testino, L. Wahba and F. Morazzoni, *Chem. Mater.*, 2010, **22**, 4083–4089.

41 Y.-d. Wang, C.-l. Ma, X.-d. Sun and H.-d. Li, *Nanotechnology*, 2002, **13**, 565–569.

42 F. Song, H. Su, J. Han, W. M. Lau, W.-J. Moon and D. Zhang, *J. Phys. Chem. C*, 2012, **116**, 10274–10281.

43 M. D'Arienzo, L. Armelao, C. M. Mari, S. Polizzi, R. Ruffo, R. Scotti and F. Morazzoni, *J. Am. Chem. Soc.*, 2011, **133**, 5296–5304.

44 X. Xue, Z. Chen, C. Ma, L. Xing, Y. Chen, Y. Wang and T. Wang, *J. Phys. Chem. C*, 2010, **114**, 3968–3972.

45 R. Dolbec and M. A. El Khakani, *Appl. Phys. Lett.*, 2007, **90**, 173114–173116.

46 H. Windischmann and P. Mark, *J. Electrochem. Soc.*, 1979, **126**, 627–633.

47 S. Kattel, W. Yu, X. Yang, B. Yan, Y. Huang, W. Wan, P. Liu and J. G. Chen, *Angew. Chem., Int. Ed.*, 2016, **128**, 8100–8105.

48 F. Calle-Vallejo, J. Tymoczko, V. Colic, Q. H. Vu, M. D. Pohl, K. Morgenstern, D. Loffreda, P. Sautet, W. Schuhmann and A. S. Bandarenka, *Science*, 2015, **350**, 185–189.

49 J.-W. Yoon, J.-S. Kim, T.-H. Kim, Y. J. Hong, Y. C. Kang and J.-H. Lee, *Small*, 2016, **12**(31), 4229–4240.

50 Q. Lipeng, X. Jiaqiang, D. Xiaowen, P. Qingyi, C. Zhixuan, X. Qun and L. Feng, *Nanotechnology*, 2008, **19**, 185705.

51 S. Tian, F. Yang, D. Zeng and C. Xie, *J. Phys. Chem. C*, 2012, **116**, 10586–10591.

52 Y. Xiao, L. Lu, A. Zhang, Y. Zhang, L. Sun, L. Huo and F. Li, *ACS Appl. Mater. Interfaces*, 2012, **4**, 3797–3804.

53 A. Katoch, S. W. Choi, G. J. Sun and S. S. Kim, *J. Nanosci. Nanotechnol.*, 2015, **15**, 438–445.

54 I. Elmi, S. Zampolli, E. Cozzani, F. Mancarella and G. Cardinali, *Sens. Actuators, B*, 2008, **135**, 342–351.

55 M. Yao, P. Hu, N. Han, F. Ding, C. Yin, F. Yuan, J. Yang and Y. Chen, *Sens. Actuators, B*, 2013, **186**, 614–621.